

Tentative detection of the circumgalactic medium of the isolated low-mass dwarf galaxy WLM

Yong Zheng^{1,2★}, Mary E. Putman,³ Andrew Emerick,^{3,4} Kristen B. W. McQuinn,^{5,6} Jessica K. Werk,⁷ Felix J. Lockman,⁸ Benjamin D. Oppenheimer,⁹ Andrew J. Fox,¹⁰ Evan N. Kirby¹¹ and Joseph N. Burchett¹²

¹Department of Astronomy, University of California, Berkeley, Berkeley, CA 94720, USA

²Miller Institute for Basic Research in Science, University of California, Berkeley, Berkeley, CA 94720, USA

³Department of Astronomy, Columbia University, New York, NY 10027, USA

⁴Department of Astrophysics, American Museum of Natural History, New York, NY 10024, USA

⁵Department of Astronomy, The University of Texas at Austin, Austin, Texas 78712, USA

⁶Department of Physics and Astronomy, Rutgers University, New Jersey, NJ 08854, USA

⁷Department of Astronomy, University of Washington, Seattle, WA 98195, USA

⁸National Radio Astronomy Observatory, Green Bank, WV 24944, USA

⁹Center for Astrophysics and Space Astronomy, Department of Astrophysical and Planetary Sciences, University of Colorado, Boulder, CO 80309, USA

¹⁰AURA for ESA, Space Telescope Science Institute, Baltimore, MD 21218, USA

¹¹Astronomy Department, California Institute of Technology, Pasadena, CA 91125, USA

¹²Department of Astronomy, University of California, Santa Cruz, CA 95064, USA

Accepted 2019 September 6. Received 2019 July 15; in original form 2019 April 3

ABSTRACT

We report a tentative detection of the circumgalactic medium (CGM) of Wolf–Lundmark–Melotte (WLM), an isolated, low-mass ($\log M_*/M_\odot \approx 7.6$), dwarf irregular galaxy in the Local Group (LG). We analyse an *HST*/COS archival spectrum of a quasar sightline (PHL2525), which is 45 kpc (0.5 virial radius) from WLM and close to the Magellanic Stream (MS). Along this sightline, two ion absorbers are detected in Si II, Si III, Si IV, C II, and C IV at velocities of ~ -220 km s⁻¹ (Component v-220) and ~ -150 km s⁻¹ (Component v-150). To identify their origins, we study the position–velocity alignment of the components with WLM and the nearby MS. Near the magellanic longitude of PHL2525, the MS-related neutral and ionized gas moves at $\lesssim -190$ km s⁻¹, suggesting an MS origin for Component v-220, but not for Component v-150. Because PHL2525 passes near WLM and Component v-150 is close to WLM’s systemic velocity (~ -132 km s⁻¹), it is likely that Component v-150 arises from the galaxy’s CGM. This results in a total Si mass in WLM’s CGM of $M_{\text{Si}}^{\text{CGM}} \sim (0.2 - 1.0) \times 10^5 M_\odot$ using assumption from other COS dwarf studies. Comparing $M_{\text{Si}}^{\text{CGM}}$ to the total Si mass synthesized in WLM over its lifetime ($\sim 1.3 \times 10^5 M_\odot$), we find ~ 3 per cent is locked in stars, ~ 6 per cent in the ISM, ~ 15 – 77 per cent in the CGM, and the rest (~ 14 – 76 per cent) is likely lost beyond the virial radius. Our finding resonates with other COS dwarf galaxy studies and theoretical predictions that low-mass galaxies can easily lose metals into their CGM due to stellar feedback and shallow gravitational potential.

Key words: techniques: spectroscopic – galaxies: dwarf (WLM) – galaxies: haloes – quasars: absorption lines.

1 INTRODUCTION

At redshift ~ 0 , only ~ 10 – 20 per cent of the baryons predicted by Λ cold dark matter (Λ CDM) cosmology (Planck Collaboration

XIII 2016) are found in stars and the interstellar medium (ISM) of galaxies (Persic & Salucci 1992; Behroozi, Conroy & Wechsler 2010; McGaugh et al. 2010; Peebles et al. 2014). In addition, hot gas in clusters and groups, as detected in X-ray, contributes ~ 4 per cent of the predicted baryons (Fukugita & Peebles 2004; Bregman 2007). The rest of the baryons, a.k.a the missing baryons, are likely to reside in the circumgalactic medium (CGM) of galaxies, and the

★ E-mail: yongzheng@berkeley.edu

surrounding intergalactic medium (Bregman 2007; Werk et al. 2014; Danforth et al. 2016; Shull, Smith & Danforth 2012; Tumlinson, Peebles & Werk 2017). So far, baryons in the CGM have been detected using quasar (quasi-stellar object; QSO) absorption line diagnostics for a wide range of galaxy masses (e.g. dwarfs, $L \sim L_*$, and luminous red galaxies; for a non-exhaustive list: Tumlinson et al. 2011; Rudie et al. 2012; Bordoloi et al. 2014; Liang & Chen 2014; Werk et al. 2014; Burchett et al. 2016; Johnson et al. 2017; Smailagić et al. 2018). Emission-line mapping of Ly α photons near star-forming galaxies and bright QSOs have also found large haloes spanning a few tens to hundreds kpc, which could be massive baryonic reservoirs (Cantalupo et al. 2014; Hennawi et al. 2015; Borisova et al. 2016; Cai et al. 2017).

Among all the galaxies being probed, low-mass dwarf galaxies are predicted to be the least likely to retain their metals in stars or ISM due to their shallow gravitational potential. Mac Low & Ferrara (1999) show that low-mass dwarf galaxies could lose the majority of their synthesized metals to the CGM and intergalactic medium (IGM) because of supernova (SN) feedback. Christensen et al. (2018) also suggest that for galaxies with stellar mass $M_* \sim 10^7 M_\odot$, 85 per cent of their synthesized metals do not remain in the galaxies by $z = 0$. These metals are mostly transported into the CGM and beyond the virial radius through outflows. In particular, for galaxies with $M_* \lesssim 10^7 M_\odot$, the outflowing metals are mostly trapped in the CGM probably due to the weakening of star formation activities (see fig. 3 in Christensen et al. 2018). Muratov et al. (2017) show that for galaxies at $M_* \sim 10^{7-7.6} M_\odot$, 50 per cent of all the metals (by mass) reside in the CGM, more than 90 per cent of which is in cool phase with $T \sim 10^{4.0-4.7}$ K (see also Ma et al. 2016). Results from different simulations vary quantitatively, probably due to different treatment of feedback recipes (see Hu et al. 2017; Emerick, Bryan & Mac Low 2018, 2019 for a detailed work on the impact of high-resolution stellar feedback modelling in regulating the efficiency of outflows). Overall, they agree that, for dwarf galaxies with $6 < \log(M_*/M_\odot) < 10$, a large fraction of metals are lost into their CGM, if not further into the IGM.

Observationally, a metal deficit has been reported in a number of low-mass dwarf galaxies in the local Universe. For example, Kirby, Martin & Finlator (2011) study the metal mass contained in stars of eight gas-poor dwarf spheroidal (dSph) galaxies over stellar mass ranges of $10^{5.7-7.3} M_\odot$, and find that the galaxies have commonly lost 96 per cent to more than 99 per cent of the metals synthesized. McQuinn et al. (2015) find that Leo P, an isolated gas-rich dwarf galaxy with $M_* \sim 10^{5.7} M_\odot$, has lost 95 per cent of the oxygen produced throughout its star formation history. In addition, the QSO absorption line technique has been employed by a number of authors in search of lost metals in the CGM of dwarf galaxies. Bordoloi et al. (2014) conduct an *HST*/COS search of metals in the CGM of 43 low-mass galaxies ($M_* \approx 10^{8.2-10.2} M_\odot$) at $z \leq 0.1$. They find a covering fraction of ~ 40 per cent for C IV within the virial radius (R_{vir}), and a minimum carbon mass of $1.2 \times 10^6 M_\odot$ within $0.5R_{\text{vir}}$ (see also Liang & Chen 2014; Burchett et al. 2016).

In this article, we present our effort in searching for the CGM of Wolf–Lundmark–Melotte (WLM), a nearby, gas-rich, low-mass dwarf irregular (dIrr) galaxy. WLM moves at a heliocentric velocity of -130 km s^{-1} (Jackson et al. 2004) and $v_{\text{LSR}} = -132 \text{ km s}^{-1}$ with respect to the Local Standard of Rest (LSR). It is located on the outskirts of the Local Group at a distance of $0.93 \pm 0.03 \text{ Mpc}$ (McConnachie et al. 2005; McConnachie 2012) from the Milky Way. WLM is an isolated galaxy $\sim 210 \text{ kpc}$ away from its nearest neighbour (the Cetus dwarf spheroidal galaxy; Whiting, Hau &

Irwin 1999). The virial radii (R_{vir}) of WLM and Cetus are ~ 90 and $\sim 60 \text{ kpc}$, respectively (see below for R_{vir} definition); therefore, their haloes do not overlap. In addition, Leaman et al. (2012) find that the stellar kinematics of WLM show no sign of tidal influence, further supporting its isolation within the Local Group. Therefore, WLM is an excellent candidate to study metal distributions due to stellar feedback without apparent influence from the environment.

WLM has a stellar mass of $M_* = 4.3 \times 10^7 M_\odot$ (Jackson et al. 2007; McConnachie 2012), and an H I mass of $M_{\text{H I}} = (6.3 \pm 0.3) \times 10^7 M_\odot$ (Kepley et al. 2007; see also Huchtmeier, Seiradakis & Materne 1981; Barnes & de Blok 2004; Jackson et al. 2004). Leaman et al. (2012) estimate WLM’s dark-matter halo mass M_h based on its stellar rotation curve and line-of-sight dispersion velocity. They find $M_h(\text{ISO}) = (2.6 \pm 0.2) \times 10^{10} M_\odot$ assuming an isothermal spherical halo, and $M_h(\text{NFW}) = (8.9 \pm 0.8) \times 10^9 M_\odot$ if using an NFW profile instead. The virial radius R_{vir} , defined as the radius within which the mean density is 200 times the cosmic critical density ρ_c , is $R_{200}(\text{ISO}) = 60.5 \text{ kpc}$ and $R_{200}(\text{NFW}) = 42.0 \text{ kpc}$, respectively (see their table 3). Meanwhile, a different definition of virial radius is also often adopted, which is referred to 200 times the matter density $\rho_m \equiv \rho_c \Omega_m$ (e.g. Werk et al. 2013; Bordoloi et al. 2014; Shull 2014). In such cases, R_{200} is systemically $(\Omega_m)^{-1/3} \approx 1.48$ times higher than the one defined with Ω_c .¹ We note that, in any case, the derivation of R_{200} is highly uncertain due to uncertainties and scatter in the M_* – M_h relation (e.g. Behroozi et al. 2010; Moster et al. 2010). For instance, the COS-Halos survey (Tumlinson et al. 2013) quote an uncertainty of 50 per cent in R_{200} due to errors propagated from the M_* – M_h relation. In this work, we adopt the virial radius of WLM as $R_{200}^{\text{WLM}} \equiv R_{200}(\text{ISO}) * \Omega_m^{-1/3} = 89.7 \text{ kpc}$, which is defined with respect to the critical matter density in an isothermal spherical halo. This definition is chosen to be consistent with the one used by the COS-Dwarfs study (equation 1; Bordoloi et al. 2014), such that we can make a direct comparison between our analysis and their CGM observations (see Section 4).

WLM has an iron abundance of $[\text{Fe}/\text{H}] = -1.28 \pm 0.02 \text{ dex}$ from spectroscopic studies of red giant branch stars (Leaman et al. 2013), and a gas-phase oxygen abundance of $12 + \log(\text{O}/\text{H})_{\text{WLM}} = 7.83 \pm 0.06$ (Lee, Skillman & Venn 2005). Its current day star formation rate is $2.7 \times 10^{-4} M_\odot \text{ yr}^{-1}$ as averaged over the galaxy (Dolphin 2000). Star formation history (SFH) analysis on selected *HST*/WFPC2 fields in WLM shows that the galaxy has experienced an active star formation epoch 1–3 Gyr ago (Dolphin 2000; Weisz et al. 2014). Escaping metals, carried by outflows driven by stellar feedback, may pollute the galaxy’s CGM over Gyr time-scales, leaving traces of elements potentially detectable in ultraviolet (UV) absorption lines.

This article focuses on UV and H I 21cm observation along a QSO sightline, PHL2525, through the CGM of WLM. In Section 2, we present the archival UV spectrum of PHL2525 retrieved from the Mikulski Archive for Space Telescopes (MAST), and follow-up H I data obtained with the Green Bank Telescope (GBT). In Section 3, we investigate the origins of the UV detection based on position–velocity alignment. In Section 4, we discuss the implication on WLM’s CGM should the detected gas originate from the galaxy. We summarize in Section 5. The codes and data used in this work can be found on GitHub: [yzhenggit/Zheng19_WLMCGM.git](https://github.com/yzhenggit/Zheng19_WLMCGM.git).

¹We adopt $\Omega_m = 0.308$ from Planck Collaboration XIII (2016) cosmological parameters.

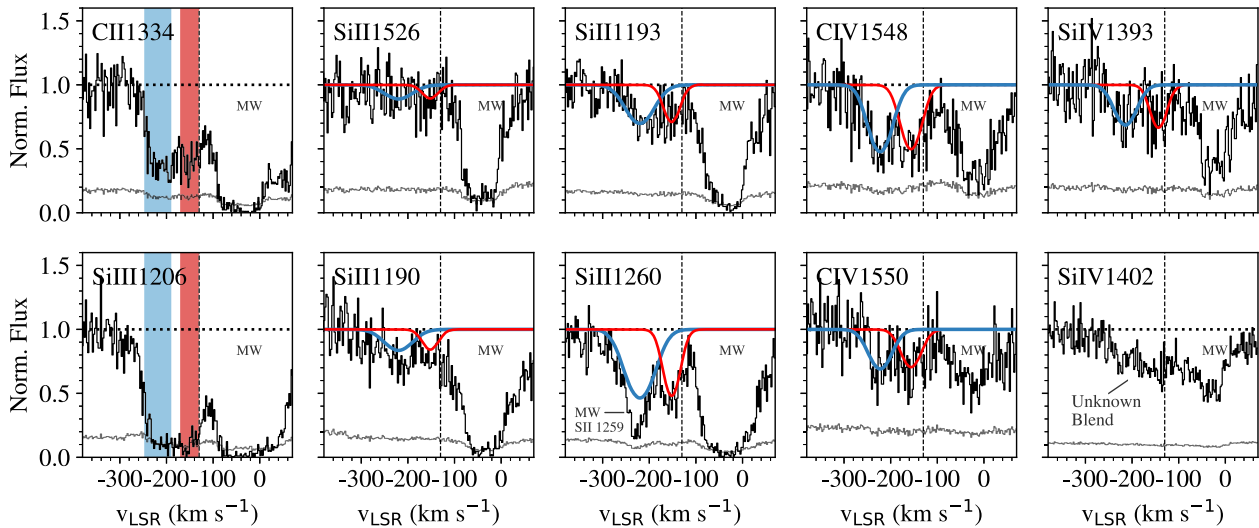


Figure 1. Detection of ion absorption lines towards PHL2525 and the corresponding Voigt-profile fits. For ions with multiple transitions, we conduct two-component fits simultaneously to all the available lines. We do not attempt to decompose the C II 1334 Å and Si III 1206 Å lines as each of them only have one transition and appears saturated. We instead measure the column densities for regions highlighted in blue and red. For each transition, we refer to the component at $v_{\text{LSR}} \sim -150 \text{ km s}^{-1}$ (red) as Component v-150, and the one at $v_{\text{LSR}} \sim -220 \text{ km s}^{-1}$ (blue) as Component v-220. We note that Si II 1260 is blended with S II 1259 from the MW’s ISM, which has been taken into account when we run the Voigt-profile fitting. See Section 2.1 for more details.

2 DATA REDUCTION AND MEASUREMENTS

2.1 *HST*/COS spectral analysis

We retrieve an *HST*/COS spectrum of QSO PHL2525 from MAST. The sightline is at RA = $00^{\text{h}}00^{\text{m}}24^{\text{s}}.42$ (0.1018 deg), Dec. = $-12^{\text{d}}45^{\text{m}}47^{\text{s}}.76$ (-12.7632 deg), and at an impact parameter of 45.2 kpc ($0.5R_{200}^{\text{WLM}}$) from WLM. The spectrum was obtained as part of GO Program 12604 (PI: A. Fox) with 2146/2772 seconds of exposure in G130M/G160M gratings, reaching a signal-to-noise ratio of 22/19, respectively (see table 1 in Fox et al. 2013, Fox13 hereafter). The spectrum has a resolution of $R \approx 16000$, corresponding to an instrumental velocity resolution of full width at half-maximum (FWHM) $\approx 19 \text{ km s}^{-1}$. To coadd the multiple x1d.fits files provided by MAST, we adopt a spectral coadding IDL code COADD_X1D.PRO developed by Danforth et al. (2010). The code works as follows. First, it randomly selects one exposure as the reference and cross-correlates the remaining exposures using strong ISM absorption lines over spectral regions of 10 Å. Once any wavelength offset is resolved among the exposures, the offset is applied to all the spectra to line up with the reference exposure wavelength. Finally, the code generates a coadded spectrum that contains exposure-weighted average flux and exposure-weighted, inverse-invariance averaged error array. We also visually inspect line features from each exposure before coaddition to make sure that the corresponding features are not due to instrumental artefacts intrinsic to the spectrograph (Rafelski & et al. 2018; COS Data Handbook, V4.0). In the following, we analyse and display the spectra in their native spectral resolution; we do not re-bin the data.

We conduct continuum normalization and Voigt-profile fitting using the software developed for the COS-Halos survey (Tumlinson et al. 2011, 2013; Werk et al. 2013, 2014; Prochaska et al. 2017). Details of the spectral analysis processes can be found in Tumlinson et al. (2013); here, we summarize the major procedures. Our analysis focuses on a number of ion absorption lines, including Si II 1190/1193/1260/1526 Å, Si III 1206 Å, Si IV 1394/1402 Å, C II 1334 Å, and C IV 1548/1550 Å. Most of the ions have multiphase

transition lines within the G130M/G160M spectral coverage, which solidify the line identification. Our data also cover O I 1302 Å, P II 1152 Å, S II 1250/1253/1259 Å, and Fe II 1142/1143/1144/1608 Å, but do not show significant detection. The non-detection limit of these lines can be found in Fox13 and Fox et al. (2014; Fox14 hereafter), and we do not use these lines in the following sections.

For each line of interest, we select a spectral region of $\pm 1000 \text{ km s}^{-1}$ within the rest wavelength for continuum normalization. We fit the absorption-line free regions with low-order Legendre polynomials until the reduced χ^2 approaches 1.0. We proceed with Voigt-profile fitting by first visually inspecting the line profiles to estimate the number of velocity components and evaluate potential contamination from intercepting absorbers at higher redshifts. We run MPFIT (Markwardt 2009) to solve for the best-fitting parameters of ion column density ($\log N$), Doppler width (b), and velocity centroid (v_c). For ions with multiple lines, Voigt-profile fitting is conducted simultaneously for all the available transition lines to ensure consistent solutions. The line spread function of COS (Ghavamian et al. 2009) has also been convolved into the fitting when we model the Voigt profiles.

We show the UV lines and Voigt-profile fitting results in Fig. 1. Each of the transitions simultaneously present two velocity components at $v_{\text{LSR}} \sim -150 \text{ km s}^{-1}$ and $\sim -220 \text{ km s}^{-1}$; hereafter, we refer to these two components as ‘Component v-150’ (colour-coded in red) and ‘Component v-220’ (colour-coded in blue) according to their LSR velocity measurements, respectively. For C II and Si III, we do not attempt to decompose the line profiles because there is only one saturated transition for each ion. In this case, the Voigt-profile fitting is highly uncertain. Instead, we define a spectral region of $-150.2 \pm (41.0/2) \text{ km s}^{-1}$ equivalent to Component v-150. The region’s centre at $v_{\text{LSR}} = -150.2 \text{ km s}^{-1}$ and its width of 41.0 km s^{-1} are from the mean v_c and FWHM ($\equiv 1.667b$) measured from the corresponding Si II, Si IV, and C IV components. Similarly, we define a spectral region of $-218.7 \pm (58.0/2) \text{ km s}^{-1}$ in C II and Si III as Component v-220. We then estimate $\log N$ for both components in C II and Si III using the apparent optical depth (AOD)

Table 1. Ion line measurements.

Ion	$\log N$ $\log(\text{cm}^{-2})$ (1)	v_c (km s^{-1}) (2)	b (km s^{-1}) (3)
Component v-150			
H I	$\leq 18.02 (3\sigma)$	–	–
C II	13.93 ± 0.04	–	–
C IV	13.67 ± 0.09	-156.0 ± 4.8	28.4 ± 6.7
Si II	12.97 ± 0.07	-151.7 ± 2.4	22.4 ± 3.3
Si III	13.30 ± 0.09	–	–
Si IV	12.95 ± 0.10	-143.2 ± 4.3	23.0 ± 6.6
Component v-220			
H I	$\leq 18.05 (3\sigma)$	–	–
C II	14.07 ± 0.03	–	–
C IV	13.75 ± 0.07	-222.2 ± 4.9	32.7 ± 6.2
Si II	13.22 ± 0.05	-220.0 ± 3.3	40.2 ± 5.8
Si III	13.36 ± 0.07	–	–
Si IV	13.05 ± 0.09	-214.0 ± 5.2	31.5 ± 8.0

Notes. Column (1): Column density. For C IV, Si II, and Si IV, $\log N$ is measured from Voigt-profile fitting. For C II and Si III, $\log N$ is integrated over a certain velocity range with AOD method (Savage & Sembach 1991, 1996). For Component v-150, the integration range is $v_{\text{LSR}} = -150.2 \pm (41.0/2) \text{ km s}^{-1}$, where -150.2 km s^{-1} is the mean centroid velocity from Si II, Si IV, and C IV, and 41.0 km s^{-1} is the mean FWHM ($\equiv 1.667b$). For Component v-220, the integration range is $v_{\text{LSR}} = -218.8 \pm (58.0/2) \text{ km s}^{-1}$ defined in a consistent way. H I column density is measured over the same velocity range as C II and Si III using GBT spectrum from pointing 1 (see Section 2.2). Column (2): Centroid velocity for C IV, Si II, and Si IV from Voigt-profile fitting, in LSR frame. Column (3): Doppler width for C IV, Si II, and Si IV from Voigt-profile fitting.

method (Savage & Sembach 1991, 1996). We tabulate the ($\log N$, b , v_c) results in Table 1.

We note that Fox13 and Fox14 have studied the UV absorbers along PHL2525 in the context of Magellanic Stream (MS; see Section 3). They measure $\log N$ for related absorbers with the AOD method over an integration range of $v_{\text{LSR}} = [-280, -120] \text{ km s}^{-1}$, which covers both Components v-150 and v-220. We compare their $\log N$ estimates with the combined values of the two components listed in Table 1, and find that they are consistent within 0.11 dex despite the different methods and velocity ranges being adopted. Neither of us finds significant detection in S II and Fe II. Fox13 also report a potential detection of O I 1302 Å with an upper limit of $\log N < 14.30$ at 3σ . Since it is a single line and only an upper limit is inferred from the data, we do not include this line in our analysis.

2.2 GBT observations and ancillary data

To study the gaseous environment near PHL2525 and WLM, we generate H I column density (N_{HI}) and flux-weighted velocity maps using the HI4PI data set (HI4PI Collaboration et al. 2016), which is an all-sky H I 21 cm survey with angular resolution of $\theta_{\text{FWHM}} = 16.2$ arcmin. Assuming the H I line is optically thin, the column density is calculated as $N(\text{H I}) \equiv 1.823 \times 10^{18} [\text{cm}^{-2} (\text{K km s}^{-1})^{-1}] \int T(v) dv$ (Dickey & Lockman 1990), and the flux-weighted velocity as $\bar{v} \equiv \int v T(v) dv / \int T(v) dv$ (km s^{-1}). We integrate the HI4PI data from $v_{\text{LSR}} = -250$ to -120 km s^{-1} to include both the MS and part of the WLM emission² as shown in Fig. 2. The noise level averaged over 1 km s^{-1} is $\sigma_T \sim 53 \text{ mK}$ (HI4PI Collaboration et al. 2016; also

²The H I emission from WLM spreads over a range of $v_{\text{LSR}} \sim -170$ to $\sim -80 \text{ km s}^{-1}$ (see fig. 7 in Kepley et al. 2007).

see table 1 in Peek et al. 2018); over a range of 130 km s^{-1} , the N_{HI} map has a sensitivity of $\sigma_{\text{HI}} = 1.823 \times 10^{18} \times 0.053 \times \sqrt{130} = 1.1 \times 10^{18} \text{ cm}^{-2}$ at 1σ (or $3.3 \times 10^{18} \text{ cm}^{-2}$ at 3σ). Within 1 deg PHL2525 (see below for GBT pointings), we find a peninsular-shape H I feature extending from the main body of the MS with $\log N_{\text{HI}} \lesssim 19.0$ (left-hand panel) and $v_{\text{LSR}} \sim -250 \text{ km s}^{-1}$ (right-hand panel), which is close to the velocity of Component v-220 from UV spectra. We do not find any prominent H I emission at $v_{\text{LSR}} \gtrsim -200 \text{ km s}^{-1}$ that are consistent with Component v-150.

To examine the H I structure near WLM and PHL2525 at a more sensitive level, we obtain 21 cm spectra with the Robert C. Byrd Green Bank Telescope (GBT) of the Green Bank Observatory (proposal #18B-376) that has a beamwidth (FWHM) of 9.1 arcmin. Observations were made by frequency-switching, and were calibrated and corrected for stray radiation as described in Boothroyd et al. (2011). Final spectra cover -560 to $+660 \text{ km s}^{-1}$ at a velocity resolution of 1.21 km s^{-1} . We observe sightlines towards WLM and PHL2525 directly, and use another 12 pointings on a coarse 30 arcmin grid to probe the H I environment near the QSO sightline (see Figs 2 and 3). Towards PHL2525 (pointing 1) the root-mean-square noise level is 8.1 mK, giving a 3σ detection limit for a 25 km s^{-1} line of $2.2 \times 10^{17} \text{ cm}^{-2}$. The median noise level for the other directions (pointings 2–13) is 16 mK, giving a 3σ limit of $4.4 \times 10^{17} \text{ cm}^{-2}$. As shown in Fig. 3, there is significant H I 21 cm emission towards pointing 4, 5, 6, 8, 10, and 11. Gaussian fitting to these emission lines finds peak-flux velocities at $\sim [-190, -270] \text{ km s}^{-1}$. The locations of GBT detection and the velocities are coincident with the peninsular-shape H I feature shown in the N_{HI} map from HI4PI (see the right-hand panel in Fig. 3).

For PHL2525 (pointing 1), we find an H I upper limit of $\log N \leq 18.05 (3\sigma)$ for Component v-220 over $v_{\text{LSR}} = -218.8 \pm (58.0/2) \text{ km s}^{-1}$, and $\log N \leq 18.02 (3\sigma)$ for Component v-150 over $v_{\text{LSR}} = -150.2 \pm (41.0/2) \text{ km s}^{-1}$ (see Table 1 for explanation of the components' velocity ranges). A weak feature may exist near $v_{\text{LSR}} \sim -260 \text{ km s}^{-1}$ with $\log N \sim 18.23$ over a velocity range of 30 km s^{-1} , consistent with the one detected in Fox13 using the LAB data set (Kalberla et al. 2005). Fox13 relates this feature to the UV absorption of Components v-150 and v-220 despite a velocity offset of $\gtrsim 50 \text{ km s}^{-1}$. They suggest that the velocity mismatch is due to the large beam size (36 arcmin) of the LAB data. However, our higher-resolution HI4PI/GBT data suggest that the beam size is unlikely to be the culprit. In the next section, we argue that gas with different origins may result in such velocity mismatch.

3 ORIGINS OF UV ABSORBERS

PHL2525 is 45.2 kpc from WLM in projection (see Fig. 2). As described in Section 1, we adopt the virial radius of WLM as $R_{200}^{\text{WLM}} = 89.7 \text{ kpc}$; therefore, PHL2525 is at $0.5 R_{200}^{\text{WLM}}$ in WLM's CGM. Alternatively, the sightline passes through the edge of the MS, which is a 100-deg long H I structure originating from the Large and Small Magellanic Clouds (Putman et al. 2003; Nidever, Majewski & Butler Burton 2008). Due to this proximity, it is possible that the two UV components originate either from MS-related gas or from ionized gas in the CGM of WLM. Here, we explore these two possible origins separately.

3.1 MS origin

In fact, Fox13 and Fox14 included PHL2525 in their UV absorption survey to study MS's ionized extension, broadly defined as areas

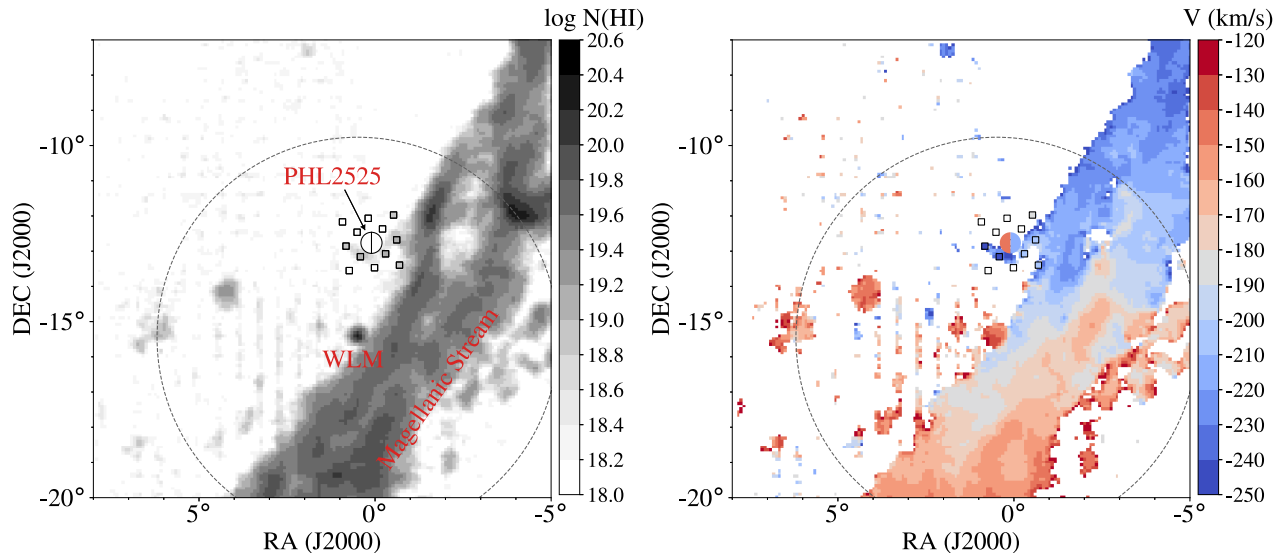


Figure 2. Left: HI column density (N_{HI}) map of WLM and its nearby MS environment. The map is integrated from $v_{\text{LSR}} = -250$ to -120 km s^{-1} using HI4PI data set (HI4PI Collaboration et al. 2016). The QSO PHL2525, at an impact parameter of 45.2 kpc ($0.5R_{200}^{\text{WLM}}$), is noted with two wedges, representing the UV absorbers of Components v-150 and v-220 along the line of sight. 12 GBT pointings, as shown in squares, are observed surrounding PHL2525 in spacing of 30 arcmin. One additional pointing directly on the QSO is not shown for clear illustration. Right: Flux-weighted velocity over the same velocity range. The colours of the wedges indicate v_{LSR} values of Components v-150 and v-220. The GBT pointings are colour-coded by the corresponding velocity when there is a detection; if none, we use white (see Fig. 3 for GBT spectra). The pointing towards the QSO does not have a detection in HI emission (see Section 2.1 for more details). The dotted circle in both maps shows the R_{200}^{WLM} radius of WLM.

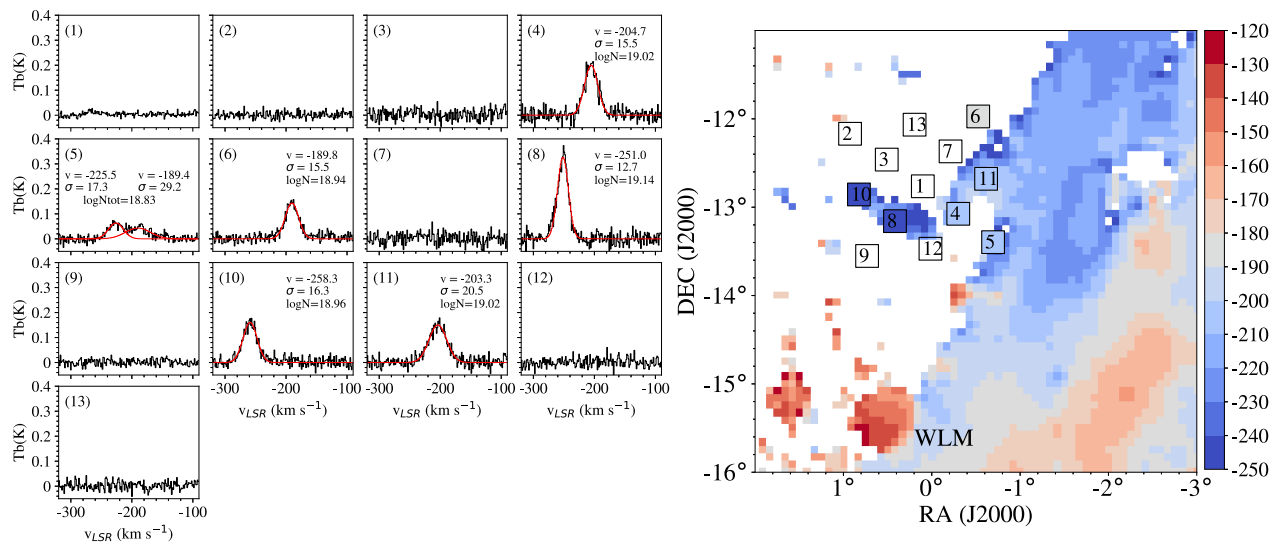


Figure 3. HI 21 cm spectra observed with GBT along PHL2525 (pointing 1) and near the QSO in spacing of 30 arcmin (pointings 2–13). We fit pointing 4, 6, 8, 10, and 11 with single Gaussian and fit pointing 5 with double Gaussians. The fitted velocity v , velocity dispersion σ , and HI column density $\log N$ are also indicated accordingly; typical fitting errors are ~ 0.5 km s^{-1} for v and σ , and 0.01 dex for $\log N$. The right-hand panel is a zoom-in version of the velocity panel in Fig. 2, with pointing number labelled consistently with the panel number on the left. In this figure, point 1 is directly towards PHL2525, which is not shown in Fig. 2. For pointing 4, 6, 8, 10, and 11, the symbols are colour-coded by the velocities of Gaussian fits; for pointing 5, a mean velocity of the two Gaussians are adopted.

within 30 deg of HI-bright regions of the MS (see fig. 1 in Fox14). In their study, a spectral region of $-280 \leq v_{\text{LSR}} \leq -120$ km s^{-1} is assumed for MS-related gas along PHL2525, covering both Components v-150 and v-220. Here, we re-evaluate the relation of both components to the MS focusing on their position–velocity alignment. We do not rely on a metallicity estimate, given the lack

of significant HI detection that would introduce a large uncertainty due to an unknown total hydrogen content.

In Fig. 4, we compare the positions and velocities of the two components with nearby HI emission and QSO absorption line measurements. Nidever et al. (2008) conducted Gaussian decomposition of HI emission lines from the MS observed with the LAB

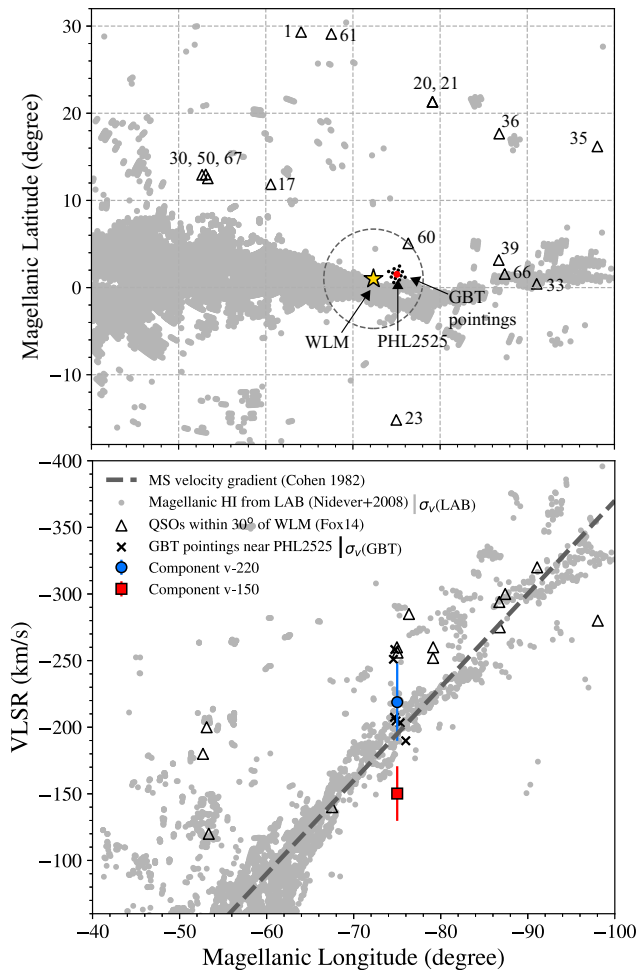


Figure 4. Position–velocity diagram for H I and ionized gas near WLM. In both panels, grey dots are H I 21 cm measurements of the MS (Nidever et al. 2008), and black open triangles are ion absorbers detected along QSO sightlines within 30 deg of WLM by Fox14. In the top panel, we plot WLM as a yellow star, PHL2525 as a red dot, and the GBT pointings near PHL2525 as smaller black dots. The large dashed circle indicates the virial radius of WLM. The numbers near the QSOs are target IDs assigned in Fox14. PHL2525 is ID 41 in their work. In the bottom panel, we show the H I detection from the GBT pointings (see Fig. 3) as black crosses. The blue dot is for Component v-220 and the red square for Component v-150, both with error bars from the Voigt-profile fitting (see Table 1). For clear illustration, we indicate the median error for the GBT H I detection ($\sigma_v = 16.3 \text{ km s}^{-1}$) as a black vertical line and that of the LAB H I detection ($\sigma_v = 14.8 \text{ km s}^{-1}$) as a grey line in the figure legend. No error bars are given for the ion absorbers (triangles) in Fox14. We also plot the MS velocity gradient ($dv/dl_{\text{MS}} \sim 7 \text{ km s}^{-1} \text{ deg}^{-1}$; Cohen 1982; Putman et al. 2003; Nidever et al. 2010) as a thick long-dashed line.

survey (Kalberla et al. 2005). The Magellanic longitudes, latitudes,³ and the Gaussian-fitted centroid velocities are plotted as grey dots in the figure. We search for QSOs within 30 deg of WLM and find 15 sightlines in addition to PHL2525 from Fox14; these 15

³The Magellanic longitude L_{MS} and latitude B_{MS} are defined by Nidever et al. (2008) as the MS coordinate system. In this system, the LMC is at $L_{\text{MS}} = 0$ and the MS extends from $L_{\text{MS}} = 0$ to $L_{\text{MS}} < -100$ deg. Gas to the north of the MS is at $B_{\text{MS}} > 0$ degree and those to the south is at $B_{\text{MS}} < 0$ deg.

sightlines are shown as black open triangles. Fox14 analysed the *HST*/COS archival spectra for these sightlines and determined MS-related centroid velocities based on either H I emission (if any) or the strongest absorption components detected along the lines of sight. As shown in the bottom panel, near the Magellanic longitude of PHL2525 ($l_{\text{MS}} = 75^\circ$), the MS-related absorbers all lie either on the MS main body or in regions with more negative velocities ($\lesssim -190 \text{ km s}^{-1}$) where H I debris is scattered. Moreover, the H I emission detected near PHL2525 through the GBT pointings also show velocities consistent with the MS. No H I emission is detected at the velocity of Component v-150.

We find that the location of Component v-220 (blue circle) in the bottom panel coincides with the Magellanic H I emission and UV absorption. However, Component v-150 (red square) is substantially below the Magellanic main body, showing an opposite trend from the ion absorbers detected in other nearby QSOs, which are located *above* the main body of the Stream in the p - v diagram. Based on the position-velocity alignment, Component v-220 is most likely to originate from the MS, while Component v-150 arises from a non-Magellanic origin.

Line ratio diagnostics are often used to study physical properties of ionized gas (e.g. Fox et al. 2011; Wakker et al. 2012; Werk et al. 2016). We find that Component v-150 has line ratios of $\log(N_{\text{Si IV}}/N_{\text{Si II}}) = -0.02 \pm 0.12$, $\log(N_{\text{Si III}}/N_{\text{Si II}}) = 0.33 \pm 0.11$, and $\log(N_{\text{C IV}}/N_{\text{C II}}) = -0.26 \pm 0.10$ dex, whereas those of Component v-220 are -0.17 ± 0.10 , 0.14 ± 0.09 , and -0.32 ± 0.08 dex, respectively. The line ratios of Component v-150 is marginally higher than those of Component v-220 by 0.1–0.2 dex (~ 1 – 2σ). For the MS gas, Fox14 measure the line ratios as a function of Magellanic longitude l_{MS} (Nidever et al. 2008). PHL2525 is at $l_{\text{MS}} = -75.0$ deg. They report a broad-line ratio range for the MS gas at a similar longitude as PHL2525: $\log(N_{\text{Si IV}}/N_{\text{Si II}}) \sim [-0.5, 0.2]$, $\log(N_{\text{Si III}}/N_{\text{Si II}}) \sim [-0.6, 0.4]$, and $\log(N_{\text{C IV}}/N_{\text{C II}}) \sim [-0.9, 0.4]$ (see fig. 4 and table 2 in Fox14). The line ratios for both of Components v-150 and v-220 are within the quoted Magellanic range. Given the broad Magellanic range and the uncertainties involved, the line ratios are inconclusive with regard to membership identification.

Overall, the position–velocity analysis of nearby Magellanic H I emission and ion absorbers indicate a Magellanic velocity range that accounts for Component v-220 but not Component v-150. Furthermore, Component v-220 is $\delta v \sim 90 \text{ km s}^{-1}$ from WLM’s systemic velocity, which is much higher than the escape velocity of the galaxy’s halo ($v_{\text{esc}} \sim 50 \text{ km s}^{-1}$). Therefore, it is unlikely that Component v-220 resides in the CGM of WLM.

Lastly, we consider the case that the absorbers lie in the CGM of the Milky Way (MW) and in the foreground of the MS. As shown in Figure 1, the absorption caused by the MW’s CGM can be found at $v_{\text{LSR}} \gtrsim -100 \text{ km s}^{-1}$, and no apparent H I high-velocity cloud exists along the direction of PHL2525 besides the Magellanic Stream at $v_{\text{LSR}} \lesssim -200 \text{ km s}^{-1}$, as shown in the sensitive GBT pointings in Figure 3 (see also Putman, Peek & Joung. 2012). Based on this mismatch in H I and UV detection, we consider it a low probability that both or either of the components are related to nearby gas structures in the MW. However, we note that, the covering fraction of ionized high-velocity ($90 < |v_{\text{LSR}}| < 170 \text{ km s}^{-1}$) gas detected in UV in the MW is much higher ($\sim 68\%$; Lehner et al. 2012, see also Richter et al. 2017) than that of the high-velocity H I emission ($\sim 37\%$; Murphy, Lockman & Savage 1995, Putman et al. 2012). Detailed examination on the connection between ionized gas and H I gas near the MS region is needed and deferred to an upcoming investigation.

3.2 WLM's CGM origin

The centroid velocity of Component v-150 differs from that of Component v-220 by $\delta_v \sim 70 \text{ km s}^{-1}$. Such a high velocity difference is unlikely to be caused by the velocity scatter of shredded MS debris clouds as we have seen from the UV and H I data. Because PHL2525 is at $0.5R_{200}^{\text{WLM}}$ from WLM, here we explore the possibility that Component v-150 is a detection of the CGM of the galaxy. WLM moves at $v_{\text{LSR}} \sim -132 \text{ km s}^{-1}$; in the galaxy's reference frame, Component v-150 moves at $\sim 20 \text{ km s}^{-1}$, which is faster than the escape velocity of the galaxy ($v_{\text{esc}} \sim 17 \text{ km s}^{-1}$) but slower than that of the dark matter halo ($v_{\text{esc}} \sim 50 \text{ km s}^{-1}$). Therefore, Component v-150 can be well retained in the CGM of WLM.

SFH analysis of WLM has shown that the galaxy experienced an active star-forming phase 1–3 Gyr ago (Dolphin 2000; Weisz et al. 2014). Supposing the metals ejected due to stellar feedback during this phase travel into the CGM at $\sim 20 \text{ km s}^{-1}$ and there is no significant velocity loss, we would find the gas at $R \sim 20\text{--}60 \text{ kpc}$ at the current time, bracketing the location of Component v-150 in WLM's CGM. Additionally, we find $\log N_{\text{CIV}} = 13.67$ for this absorber (see Table 1). This value is consistent with the estimate by the COS-Dwarf survey (Bordoloi et al. 2014) that detects C IV absorption out to $\sim 0.5R_{\text{vir}}$ at $\log N_{\text{CIV}} \sim 13.7$, although we note that WLM has a lower stellar mass than those in the dwarf sample studied by Bordoloi et al. (2014).

4 DISCUSSION: WLM'S SILICON BUDGET

In this section, we first focus on the implication of Component v-150 in the context of WLM's CGM (Section 4.1), then estimate the silicon (Si) mass budget in stars, ISM, CGM, and IGM accordingly in Section 4.2.

4.1 Silicon in WLM's CGM

Because multiple silicon and carbon ions are simultaneously detected whereas there is no trace of H I at a sensitivity of $\log N_{\text{HI}} \gtrsim 18.02$ at 3σ , the CGM of WLM should be well-ionized and metal-enriched. Assuming that Si is mostly in the forms of Si II, Si III, and Si IV to the zeroth order, we can solve for the total Si mass contained in WLM's CGM as the following. From Table 1, we find that the total Si column density at $0.5R_{200}^{\text{vir}}$ is $\log N_{\text{Si}} \equiv \log N_{\text{Si II} + \text{Si III} + \text{Si IV}} = 13.6$ as measured from Component v-150. Assuming a constant density profile in WLM's CGM, we have

$$M_{\text{Si,0th}}^{\text{CGM}} = \pi (R_{200}^{\text{WLM}})^2 m_{\text{Si}} N_{\text{Si}} C_f \approx 2 \times 10^4 M_{\odot} \left(\frac{N_{\text{Si}}}{10^{13.6} \text{ cm}^{-2}} \right) \left(\frac{R_{200}^{\text{WLM}}}{89.6 \text{ kpc}} \right)^2 \left(\frac{C_f}{0.4} \right), \quad (1)$$

where C_f is the covering fraction (i.e. detection rate). Because we only have one sightline through the halo, adopting a C_f value of unity is unpractical. There are currently no observational constraints on the C_f value of Si in WLM's mass range. The best comparison point is the C IV survey by the COS-dwarfs team (Bordoloi et al. 2014) that covers dwarf mass range of $M_* \sim 10^{8.2\text{--}10.2} M_{\odot}$. We assume that their results can be extrapolated to WLM's mass and that Si II, Si III, Si IV, and C IV co-exist in a multiphase medium. We find $C_f \approx 0.4$.⁴

⁴ 17 of the 43 QSO sightlines from the COS-Dwarf sample (Bordoloi et al. 2014) show detection or lower limits of C IV.

Assuming a constant density profile in Equation (1) may not best represent the nature of the gas distribution in WLM's CGM. As pointed out by Oh et al. (2015), the mass distribution of dwarf galaxies observed in the LITTLE THINGS survey (Hunter et al. 2012) tends to have a smoother isothermal profile than an NFW profile. With the large uncertainty of the matter density distribution in dwarf galaxies in mind, we can refine the $M_{\text{Si,0th}}^{\text{CGM}}$ value by calculating the mass over the whole halo in an annular manner; the method is also commonly adopted to estimate the CGM mass for extragalactic systems (e.g. Werk et al. 2014; Peebles et al. 2014; Lehner, Howk & Wakker 2015; Prochaska et al. 2017). Taking $N_{\text{Si}}(r)$ as the Si column density profile and $C_f(r)$ the covering fraction profile, we have

$$M_{\text{Si,refined}}^{\text{CGM}} = \int_0^{R_{200}^{\text{WLM}}} m_{\text{Si}} N_{\text{Si}}(r) C_f(r) 2\pi r dr \sim 1 \times 10^5 M_{\odot}. \quad (2)$$

In this calculation, we again use the C IV measurements from the COS-Dwarfs survey (Bordoloi et al. 2014) as a proxy to derive $N_{\text{Si}}(r)$ and $C_f(r)$ profile assuming a multiphase medium. Using all of the detections found in their table 1 (and treating lower limits as detection as well), we find a power-law distribution of $N_{\text{CIV}}(r) \propto (r/R_{\text{vir}})^{-1.6}$. Normalizing this profile at $r/R_{\text{vir}} = 0.5$ with $\log N_{\text{Si}} = 13.6$ for WLM's CGM, we have $N_{\text{Si}}(r) = 10^{13.1} (r/R_{\text{vir}})^{-1.6}$. Similarly, for the covering fraction profile, we find, $C_f(r/R_{\text{vir}} \leq 0.2) = 0.9$, $C_f(0.2 < r/R_{\text{vir}} \leq 0.4) = 0.5$, and $C_f(0.4 < r/R_{\text{vir}} \leq 0.6) = 0.2$ from their data; beyond $0.6R_{\text{vir}}$, the C IV detection rate drops to zero. Because we only aim for a coarse estimate, therefore, we do not take into account the detection limit when estimating $C_f(r)$ from their data. We note that both $M_{\text{Si,0th}}^{\text{CGM}}$ and $M_{\text{Si,refined}}^{\text{CGM}}$ are only as accurate as order-of-magnitude estimates given the assumptions that go into the calculations. The major sources of uncertainties in our calculation are from the virial radius of the galaxy's dark matter halo, the Si density profile, and the covering fraction. In the following, we adopt $M_{\text{Si}}^{\text{CGM}} = (0.2 - 1) \times 10^5 M_{\odot}$ that incorporates both of the calculations in equations (1) and (2). In Table 2, we record the $M_{\text{Si}}^{\text{CGM}}$ value as well as other mass estimates described as follows.

4.2 Silicon in stars and ISM

We can compare $M_{\text{Si}}^{\text{CGM}}$ with the total amount of Si that has ever been produced in WLM using stellar evolution models and SFH analysis. A similar technique is also used by Telford et al. (2018) to estimate the metal loss from M31. Assuming a Kroupa initial mass function (IMF; Kroupa 2002) with a minimum stellar mass of $0.08 M_{\odot}$ and a maximum of $100 M_{\odot}$ at the metallicity of WLM, we find that the fraction of mass returned to the ISM per stellar generation is $R = 0.34$. The net stellar yield of Si is $y_{\text{Si}} \sim 0.003$, which is defined as the ratio of Si mass produced and available in gas to the amount of mass locked in stars, $y_{\text{Si}} = M_{\text{Si}}^{\text{gas}}/M_*$ (also see equation 2, Vincenzo et al. 2016). The values of R and f_{Si} are calculated using the NuGrid collaboration yield set (Ritter et al. 2018b) and the SYGMA simple stellar population model (Ritter et al. 2018a). Detailed calculations with different choices of IMF, stellar mass range, and metallicity are shown in the Appendix and Table A1. We find that R is not sensitive to the choice of metallicity – it only varies by ~ 2 per cent from $Z = 0.0001$ to $0.02 Z_{\odot}$. However, choosing a Salpeter IMF (Salpeter 1955) would reduce the value by ~ 35 per cent from $R \approx 0.34$ to $R \approx 0.23$. On the other hand, the stellar yield y_{Si} does not vary significantly with different IMFs, but is sensitive to the choice of metallicity. We expect a variation of ~ 30 per cent from $Z = 0.0001$ to $0.02 Z_{\odot}$. We also consider the

Table 2. Silicon mass estimates for WLM.

	Name	Mass (M_{\odot})	Note
(1)	M_*	4.3×10^7	Stellar mass (Jackson et al. 2007).
(2)	M_{HI}	$(6.3 \pm 0.3) \times 10^7$	H I mass (Kepley et al. 2007); total gas mass in the ISM including He is $\sim 8.5 \times 10^7 M_{\odot}$.
(3)	$M_{\text{h}}(\text{ISO})$	$(2.6 \pm 0.2) \times 10^{10}$	Halo mass assuming isothermal spherical volume (Leaman et al. 2012).
(4)	$M_{\text{Si}}^{\text{CGM}}$	$\sim (0.2 - 1.0) \times 10^5$	Estimate of the CGM Si mass based on QSO absorption line data, the range is given based on the zeroth order and the refined calculations in equations (1) and (2).
(5)	$M_{\text{SF}}^{\text{tot}}$	$\sim 6.5 \times 10^7$	Total stellar mass formed throughout WLM's SFH, $M_{\text{SF}}^{\text{tot}} = M_*/(1 - R)$ (see equation 3). $R = 0.34$ is the fraction of mass returned to ISM from a stellar population, and R can vary by ~ 35 percent with different choice of IMFs and by 10–30 per cent with different stellar yield sets.
(6)	$M_{\text{Si}}^{\text{gas}}$	$\sim 1.3 \times 10^5$	Expected total Si mass in gas forms in ISM, CGM, and IGM (see equation 4). $y_{\text{Si}} = 0.003$ is the net stellar yield, and its value can vary by ~ 30 per cent due to different choice of metallicity.
(7)	$M_{\text{Si}}^{\text{ISM}}$	$(7.9 \pm 1.5) \times 10^3$	Total Si mass in ISM, based on M_{HI} and oxygen abundance of WLM's H II regions (see equation 6). $M_{\text{Si}}^{\text{ISM}}$ would be a factor of 2 higher if WLM had a similar Si depletion pattern as SMC.
(8)	M_{Si}^*	$(4.0 \pm 0.7) \times 10^3$	Total Si mass in stars, assuming the stars have similar composition as the ISM (see equation 7).
(9)	$M_{\text{Si}}^{\text{tot}}$	$\sim 1.3 \times 10^5$	Total Si mass that have been produced, $M_{\text{Si}}^{\text{tot}} = M_{\text{Si}}^{\text{gas}} + M_{\text{Si}}^*$.

influence of different yield tables by comparing our R values with those in Vincenzo et al. (2016). We find that, at a fixed IMF and metallicity, R varies by ~ 10 –30 per cent with different stellar yield sets from Romano et al. (2010), Nomoto, Kobayashi & Tominaga (2013), and Ritter et al. (2018b). In the following calculation, we proceed with $R = 0.34$ and $y_{\text{Si}} = 0.003$, and note that these values are subject to the details of different models of stellar evolution and stellar yields.

The fraction of mass locked in stars is $R_* = 1 - R = 0.66$. Since WLM has a stellar mass of $M_* = 4.3 \times 10^7 M_{\odot}$ (Jackson et al. 2007; McConnachie 2012), in total the galaxy has formed

$$M_{\text{tot}}^{\text{SF}} = M_*/(1 - R) \sim 6.5 \times 10^7 M_{\odot} \quad (3)$$

throughout its SFH. This mass estimate is consistent with the SFH analysis on combined UVIS and ACS fields in WLM by Albers et al. (2019), who show that a total amount of $M_{\text{UVIS+ACS}} \approx 7.4 \times 10^6 M_{\odot}$ has been formed over ~ 50 per cent of the area within the half-light radius ($r_{\text{h}} = 2.1$ kpc) of the galaxy (see also Weisz et al. 2014). Assuming a constant mass-to-light ratio over the whole galaxy, we find a total mass of $M_{\text{UVIS+ACS}}/0.5 \times 2 \sim 3 \times 10^7 M_{\odot}$ formed within twice the half-light radius. This value is consistent with the estimated $M_{\text{tot}}^{\text{SF}}$ value in equation (3), given the uncertainty in R . Using the net stellar yield y_{Si} , we find that the total Si mass now in the form of gas is

$$M_{\text{Si}}^{\text{gas}} = y_{\text{Si}} M_* \sim 1.3 \times 10^5 M_{\odot}, \quad (4)$$

which is expected to be in WLM's ISM, CGM, and the surrounding IGM. Note that this calculation assumes instantaneous and homogeneous mixing, which may slightly underestimate $M_{\text{Si}}^{\text{gas}}$.

Independently, we can estimate the total Si mass in WLM's ISM, $M_{\text{Si}}^{\text{ISM}}$, as the following. A similar technique is used by McQuinn et al. (2015) to estimate the oxygen mass in the ISM and stars of Leo P (see their equations 2 and 4). WLM has an oxygen abundance of $12 + \log(\text{O}/\text{H})_{\text{WLM}} = 7.83 \pm 0.06$ as measured from its H II regions (Lee et al. 2005). Assuming that WLM's ISM has a similar element composition as the Sun, despite its lower metallicity, we can estimate the Si abundance as

$$\begin{aligned} 12 + \log(\text{Si}/\text{H})_{\text{WLM}} &= \log\left[\left(\frac{\text{Si}}{\text{O}}\right)\left(\frac{\text{O}}{\text{H}}\right)\right] \\ &= \log(\text{Si}/\text{O})_{\odot} + \log(\text{O}/\text{H})_{\text{WLM}} \\ &= 6.65 \pm 0.08, \end{aligned} \quad (5)$$

where $\log(\text{Si}/\text{O})_{\odot} \equiv \log(\text{Si}/\text{H})_{\odot} - \log(\text{O}/\text{H})_{\odot}$, and we adopt Si and O solar abundance $12 + \log(\text{Si}/\text{H})_{\odot} = 7.51 \pm 0.03$ and $12 + \log(\text{O}/\text{H})_{\odot} = 8.69 \pm 0.05$ from Asplund et al. (2009). Assuming that molecular gas contributes little to WLM's ISM gas mass (Rubio et al. 2015), the total Si mass in the ISM is

$$M_{\text{Si}}^{\text{ISM}} = M_{\text{HI}} \left(\frac{m_{\text{Si}}}{m_{\text{H}}}\right) 10^{\log(\text{Si}/\text{H})_{\text{WLM}}} = (7.9 \pm 1.5) \times 10^3 M_{\odot}, \quad (6)$$

where m_{Si} and m_{H} are the Si and H atomic mass numbers, respectively. In the above calculation, we assume that the amount of Si depleted in dust is negligible in WLM's ISM. This calculation may underestimate the amount of Si in the ISM by a factor of 2 if WLM followed a similar Si depletion pattern as the Small Magellanic Cloud (SMC) which has a similar metallicity as WLM. Jenkins & Wallerstein (2017) study the gas-phase abundance and element depletion of SMC's ISM using UV absorption lines of 18 stars in the galaxy, and find that that amount of Si in dust with respect to the amount of total H is $(\text{Si}_{\text{dust}}/\text{H})_{\text{SMC}} \approx 4 \times 10^{-6}$ (see their equations 1, 5 and table 3). If applicable to WLM, we would find a total mass of $M_{\text{Si}}^{\text{dust}} = (m_{\text{Si}}/m_{\text{H}}) M_{\text{HI}} (\text{Si}_{\text{dust}}/\text{H})_{\text{SMC}} \approx 7 \times 10^3 M_{\odot}$ in dust. In such case, the $M_{\text{Si}}^{\text{ISM}}$ value calculated in equation (6) should be a factor of 2 higher.

Similarly, if we assume that the stars share similar composition with the ISM, the total amount of Si locked in the stars can be calculated as

$$\begin{aligned} 12 M_{\text{Si}}^* &= M_* \frac{\rho_{\text{Si}}}{\rho_{\text{H+He}}} = M_* \frac{m_{\text{Si}} n_{\text{Si}}}{(m_{\text{H}} n_{\text{H}}/X)} = M_* \left(\frac{m_{\text{Si}}}{m_{\text{H}}}\right) \left(\frac{n_{\text{Si}}}{n_{\text{H}}}\right) X \\ &= (4.0 \pm 0.7) \times 10^3 M_{\odot}, \end{aligned} \quad (7)$$

where $X = 0.74$ is the hydrogen mass fraction and $\left(\frac{n_{\text{Si}}}{n_{\text{H}}}\right) = 10^{\log(\text{Si}/\text{H})_{\text{WLM}}}$.

In all, the total amount of Si that has been produced is $M_{\text{Si}}^{\text{tot}} = M_{\text{Si}}^{\text{gas}} + M_{\text{Si}}^* \sim 1.3 \times 10^5 M_{\odot}$. Of this mass, ~ 3 per cent ($= M_{\text{Si}}^*/M_{\text{Si}}^{\text{tot}}$) is locked in stars, ~ 6 per cent ($= M_{\text{Si}}^{\text{ISM}}/M_{\text{Si}}^{\text{tot}}$) is retained in the ISM, and ~ 15 per cent – 77 per cent ($= M_{\text{Si}}^{\text{CGM}}/M_{\text{Si}}^{\text{tot}}$) is in the CGM. The remainder Si, 14 per cent – 76 per cent, may be depleted in dust in the ISM, exist in higher ionization phases in the CGM, or have been blown out into the IGM. Dust depletion may account for another 6 per cent of the silicon as we discuss near equation (6), whereas the amount of Si at higher ionization states should be minimal. Recent simulations have shown that ~ 90 per cent of the metals in the CGM of low-mass dwarf galaxies are in cool ($T \sim 10^{4-4.7}$ K) phase that we have already probed in Si II, Si III, and Si IV (Muratov et al. 2017), as compared to a

much lower fraction (19–42 per cent) in cool phase in $\sim L^*$ galaxies (Oppenheimer et al. 2018).

To summarize, our calculation is consistent with existing observations of both Leo P (McQuinn et al. 2015) and dwarf spheroidal galaxies of the Milky Way (Kirby et al. 2011) which estimate that $\gtrsim 95$ per cent of the metals synthesized by stars in dwarf galaxies have been lost into the CGM and IGM. It also supports theoretical predictions that metals are easily lost to the CGM in low-mass galaxies through feedback-driven outflows (e.g. Mac Low & Ferrara 1999; Ma et al. 2016; Muratov et al. 2017; Christensen et al. 2018). It is beyond the scope of this work to explore further the detailed mass fraction differences between our calculation and the theoretical predictions. We note that it is challenging to determine metal mass distribution conclusively in part because the number of detailed simulations of dwarf galaxies in this mass range is limited, and the properties of simulated dwarfs at this stellar mass for a single feedback prescription exhibit noticeable variability. In addition, our CGM mass calculation is subject to observational and model-dependent uncertainties, such as the $M_* - M_h$ relation, assumed halo density profile, assumed covering fraction, and the limited studies of the CGM in dwarf galaxies at such a low-mass ($M_* \sim 10^7 M_\odot$) regime. Therefore, the reader should use caution when interpreting results from both simulations and our observation.

5 SUMMARY

We analyse an archival *HST*/COS spectrum of a QSO sightline, PHL2525, passing through the CGM of WLM at an impact parameter of 45.2 kpc (R_{200}^{WLM}). Two absorption line components are recovered with Voigt-profile fitting at $v_{\text{LSR}} \sim -220$ and $\sim -150 \text{ km s}^{-1}$ (i.e. Components v-220 and v-150). Both WLM and PHL2525 are in the vicinity of the MS in projection. We investigate the relations of Components v-220 and v-150 with the ionized extension of MS and the CGM of WLM. Our findings are summarized as the following.

First, based on the position-velocity diagram in Fig. 4, we find that at the Magellanic longitude around $l_{\text{MS}} = -75$ degree, both the neutral (HI) and ionized gas related to the MS are moving at velocities of $v_{\text{LSR}} \lesssim -190 \text{ km s}^{-1}$. The velocity of Component v-220 is consistent with that of the MS, whereas Component v-150 is beyond this range. Because PHL2525 is at $0.5 R_{200}^{\text{WLM}}$ from WLM and Component v-150 moves at $\sim 20 \text{ km s}^{-1}$ within respect to the galaxy's systemic velocity, we propose that Component v-150 arises from the CGM of WLM. SFH analysis of WLM shows that the galaxy experienced an active star-forming epoch 1–3 Gyr ago. If WLM expelled metals into the CGM during this epoch, the gas parcel would have travel to a distance of 20–60 kpc assuming a speed of 20 km s^{-1} , which is consistent with the location of Component v-150 at $R = 45.2 \text{ kpc}$ from WLM.

If Component v-150 is associated with the CGM of WLM, we find a total Si mass of $M_{\text{Si}}^{\text{CGM}} \sim (0.2 - 1.0) \times 10^5 M_\odot$ within the virial radius of the galaxy. This assumes all the silicon atoms are in the forms of Si II, Si III, and Si IV. We note that the $M_{\text{Si}}^{\text{CGM}}$ value should be treated only as an order-of-magnitude approximation with the assumptions involved. We also calculate the Si mass in the stars and ISM using stellar evolution modelling, and find $M_{\text{Si}}^* = (4.0 \pm 0.7) \times 10^3 M_\odot$ in stars and $M_{\text{Si}}^{\text{ISM}} = (7.9 \pm 1.5) \times 10^3 M_\odot$ in the ISM (see Table 2). Therefore, the Si mass fractions now in the forms of stars, ISM and CGM of WLM are ~ 3 per cent, ~ 6 per cent, and ~ 15 – 77 per cent, respectively. The rest of the Si, 14 – 76 per cent, may be depleted in the dust in the ISM, exist in higher ionization phases other than Si II, Si III, and Si IV in the CGM,

or have been blown out into the IGM. Our finding is consistent with theoretical predictions that metals can be easily expelled to the CGM in low-mass galaxies.

Because WLM is isolated from other galaxies in the LG, the detection of its CGM as revealed by Component v-150 provides an unique case to study how stellar feedback distributes metals into the CGM of low-mass dwarf galaxies without environmental influence. It supports theoretical work (e.g. Mac Low & Ferrara 1999; Ma et al. 2016; Muratov et al. 2017; Christensen et al. 2018) which predict that dwarf galaxies with $M_* \sim 10^{7-8} M_\odot$ cannot retain most of the metals they have synthesized, and that most of the lost metals would reside in the CGM at cool phases. To better understand how metals are transported through stellar feedback processes, it is of great need to conduct further observations of the CGM of low-mass dwarf galaxies in the $M_* \lesssim 10^8 M_\odot$ regime, and to include SFH analyses of the galaxies' metal production history.

ACKNOWLEDGEMENTS

YZ is grateful to D. Weisz for many useful discussions during the preparation of this work. YZ thanks S. Albers for providing SFH estimates of WLM on combined UVIS/ACS fields, thanks C. F. McKee for his feedback on this manuscript, and thanks C. howk and N. Lehner for their comments on possible origin of the MW ionized high-velocity clouds. YZ acknowledges support from the Miller Institute for Basic Research in Science. AE was supported by the National Science Foundation (NSF) Blue Waters Graduate Fellowship. ENK acknowledges support by NASA through a grant (HST-GO-15156.004-A) from the Space Telescope Science Institute, which is operated by the Association of Universities for Research in Astronomy, Incorporated, under NASA contract NAS 5-26555. The UV spectrum presented in this work was obtained from the Mikulski Archive for Space Telescopes (MAST). Facilities: *HST*/COS, Green Bank Telescope. Software: ASTROPY (Astropy Collaboration et al. 2013), IDL, NUMPY (Oliphant 2007), MATPLOTLIB (Hunter 2007).

REFERENCES

- Albers S. M. et al., 2019, preprint (arXiv:1909.04040)
 Asplund M., Grevesse N., Sauval A. J., Scott P., 2009, *ARA&A*, 47, 481
 Astropy Collaboration et al., 2013, *A&A*, 558, A33
 Barnes D. G., de Blok W. J. G., 2004, *MNRAS*, 351, 333
 Behroozi P. S., Conroy C., Wechsler R. H., 2010, *ApJ*, 717, 379
 Boothroyd A. I., Blagrove K., Lockman F. J., Martin P. G., Pinheiro Gonçalves D., Srikanth S., 2011, *A&A*, 536, A81
 Bordoloi R. et al., 2014, *ApJ*, 796, 136
 Borisova E. et al., 2016, *ApJ*, 831, 39
 Bregman J. N., 2007, *ARA&A*, 45, 221
 Burchett J. N. et al., 2016, *ApJ*, 832, 124
 Cai Z. et al., 2017, *ApJ*, 837, 71
 Cantalupo S., Arrigoni-Battaia F., Prochaska J. X., Hennawi J. F., Madau P., 2014, *Nature*, 506, 63
 Christensen C. R., Davé R., Brooks A., Quinn T., Shen S., 2018, *ApJ*, 867, 142
 Cohen R. J., 1982, *MNRAS*, 199, 281
 Danforth C. W., Keeney B. A., Stocke J. T., Shull J. M., Yao Y., 2010, *ApJ*, 720, 976
 Danforth C. W. et al., 2016, *ApJ*, 817, 111
 Dickey J. M., Lockman F. J., 1990, *ARA&A*, 28, 215
 Dolphin A. E., 2000, *ApJ*, 531, 804
 Emerick A., Bryan G. L., Mac Low M.-M., 2018, *ApJ*, 865, L22
 Emerick A., Bryan G. L., Mac Low M.-M., 2019, *MNRAS*, 482, 1304
 Fox A. J., Ledoux C., Petitjean P., Srianand R., Guimarães R., 2011, *A&A*, 534, A82

- Fox A. J., Richter P., Wakker B. P., Lehner N., Howk J. C., Ben Bekhti N., Bland-Hawthorn J., Lucas S., 2013, *ApJ*, 772, 110 (Fox13)
- Fox A. J. et al., 2014, *ApJ*, 787, 147 (Fox14)
- Fukugita M., Peebles P. J. E., 2004, *ApJ*, 616, 643
- Ghavamian P. et al., 2009, Technical Report, Preliminary Characterization of the Post-Launch Line Spread Function of COS, Space Telescope Science Institute, Baltimore, MD
- Hennawi J. F., Prochaska J. X., Cantalupo S., Arrigoni-Battaia F., 2015, *Science*, 348, 779
- HI4PI Collaboration et al., 2016, *A&A*, 594, A116
- Hu C.-Y., Naab T., Glover S. C. O., Walch S., Clark P. C., 2017, *MNRAS*, 471, 2151
- Huchtmeier W. K., Seiradakis J. H., Materne J., 1981, *A&A*, 102, 134
- Hunter D. A. et al., 2012, *AJ*, 144, 134
- Hunter J. D., 2007, *CSE*, 9, 90
- Jackson D. C., Skillman E. D., Cannon J. M., Côté S., 2004, *AJ*, 128, 1219
- Jackson D. C., Skillman E. D., Gehrz R. D., Polomski E., Woodward C. E., 2007, in Kerschbaum F., Charbonnel C., Wing R. F., eds, ASP Conf. Ser. Vol. 378, Why Galaxies Care About AGB Stars: Their Importance as Actors and Probes. Astron. Soc. Pac., San Francisco, p. 427
- Jenkins E. B., Wallerstein G., 2017, *ApJ*, 838, 85
- Johnson S. D., Chen H.-W., Mulchaey J. S., Schaye J., Straka L. A., 2017, *ApJ*, 850, L10
- Kalberla P. M. W., Burton W. B., Hartmann D., Arnal E. M., Bajaja E., Morras R., Pöppel W. G. L., 2005, *A&A*, 440, 775
- Kepley A. A., Wilcots E. M., Hunter D. A., Nordgren T., 2007, *AJ*, 133, 2242
- Kirby E. N., Martin C. L., Finlator K., 2011, *ApJ*, 742, L25
- Kroupa P., 2002, *Science*, 295, 82
- Leaman R. et al., 2012, *ApJ*, 750, 33
- Leaman R. et al., 2013, *ApJ*, 767, 131
- Lee H., Skillman E. D., Venn K. A., 2005, *ApJ*, 620, 223
- Lehner N., Howk J. C., Thom C., Fox A. J., Tumlinson J., Tripp T. M., Meiring J. D., 2012, *MNRAS*, 424, 2896
- Lehner N., Howk J. C., Wakker B. P., 2015, *ApJ*, 804, 79
- Liang C. J., Chen H.-W., 2014, *MNRAS*, 445, 2061
- Mac Low M.-M., Ferrara A., 1999, *ApJ*, 513, 142
- Markwardt C. B., 2009, in Bohlender D. A., Durand D., Dowler P., eds, ASP Conf. Ser. Vol. 411, Astronomical Data Analysis Software and Systems XVIII. Astron. Soc. Pac., San Francisco, p. 251
- Ma X., Hopkins P. F., Faucher-Giguère C.-A., Zolman N., Muratov A. L., Kereš D., Quataert E., 2016, *MNRAS*, 456, 2140
- McConnachie A. W., 2012, *AJ*, 144, 4
- McConnachie A. W., Irwin M. J., Ferguson A. M. N., Ibata R. A., Lewis G. F., Tanvir N., 2005, *MNRAS*, 356, 979
- McGaugh S. S., Schombert J. M., de Blok W. J. G., Zagursky M. J., 2010, *ApJ*, 708, L14
- McQuinn K. B. W. et al., 2015, *ApJ*, 815, L17
- Moster B. P., Somerville R. S., Maulbetsch C., van den Bosch F. C., Macciò A. V., Naab T., Oser L., 2010, *ApJ*, 710, 903
- Muratov A. L. et al., 2017, *MNRAS*, 468, 4170
- Murphy E. M., Lockman F. J., Savage B. D., 1995, *ApJ*, 447, 642
- Nidever D. L., Majewski S. R., Butler Burton W., 2008, *ApJ*, 679, 432
- Nidever D. L., Majewski S. R., Butler Burton W., Nigra L., 2010, *ApJ*, 723, 1618
- Nomoto K., Kobayashi C., Tominaga N., 2013, *ARA&A*, 51, 457
- Oh S.-H. et al., 2015, *AJ*, 149, 180
- Oliphant T. E., 2007, Python for Scientific Computing. <http://www.numpy.org/>
- Oppenheimer B. D., Schaye J., Crain R. A., Werk J. K., Richings A. J., 2018, *MNRAS*, 481, 835
- Peek J. E. G. et al., 2018, *ApJS*, 234, 2
- Peeples M. S., Werk J. K., Tumlinson J., Oppenheimer B. D., Prochaska J. X., Katz N., Weinberg D. H., 2014, *ApJ*, 786, 54
- Persic M., Salucci P., 1992, *MNRAS*, 258, 14P
- Planck Collaboration et al., 2016, *A&A*, 594, A13
- Prochaska J. X. et al., 2017, *ApJ*, 837, 169
- Putman M. E., Peek J. E. G., Jounge M. R., 2012, *ARA&A*, 50, 401
- Putman M. E., Staveley-Smith L., Freeman K. C., Gibson B. K., Barnes D. G., 2003, *ApJ*, 586, 170
- Rafelski M. et al., 2018, COS Data Handbook v. 4.0, Space Telescope Science Institute, Baltimore, MD
- Richter P. et al., 2017, *A&A*, 607, A48
- Ritter C., Côté B., Herwig F., Navarro J. F., Fryer C. L., 2018a, *ApJS*, 237, 42
- Ritter C., Herwig F., Jones S., Pignatari M., Fryer C., Hirschi R., 2018b, *MNRAS*, 480, 538
- Romano D., Karakas A. I., Tosi M., Matteucci F., 2010, *A&A*, 522, A32
- Rubio M., Elmegreen B. G., Hunter D. A., Brinks E., Cortés J. R., Cigan P., 2015, *Nature*, 525, 218
- Rudie G. C. et al., 2012, *ApJ*, 750, 67
- Salpeter E. E., 1955, *ApJ*, 121, 161
- Savage B. D., Sembach K. R., 1991, *ApJ*, 379, 245
- Savage B. D., Sembach K. R., 1996, *ARA&A*, 34, 279
- Shull J. M., 2014, *ApJ*, 784, 142
- Shull J. M., Smith B. D., Danforth C. W., 2012, *ApJ*, 759, 23
- Smailagić M., Prochaska J. X., Burchett J., Zhu G., Ménard B., 2018, *ApJ*, 867, 106
- Telford O. G., Werk J. K., Dalcanton J. J., Williams B. F., 2019, *ApJ*, 877, 120
- Tumlinson J., Peeples M. S., Werk J. K., 2017, *ARA&A*, 55, 389
- Tumlinson J. et al., 2011, *Science*, 334, 948
- Tumlinson J. et al., 2013, *ApJ*, 777, 59
- Vincenzo F., Matteucci F., Belfiore F., Maiolino R., 2016, *MNRAS*, 455, 4183
- Wakker B. P., Savage B. D., Fox A. J., Benjamin R. A., Shapiro P. R., 2012, *ApJ*, 749, 157
- Weisz D. R., Dolphin A. E., Skillman E. D., Holtzman J., Gilbert K. M., Dalcanton J. J., Williams B. F., 2014, *ApJ*, 789, 147
- Werk J. K., Prochaska J. X., Thom C., Tumlinson J., Tripp T. M., O'Meara J. M., Peeples M. S., 2013, *ApJS*, 204, 17
- Werk J. K. et al., 2014, *ApJ*, 792, 8
- Werk J. K. et al., 2016, *ApJ*, 833, 54
- Whiting A. B., Hau G. K. T., Irwin M., 1999, *AJ*, 118, 2767

APPENDIX: STELLAR EVOLUTION MODELLING

We calculate the fraction of mass returned into the ISM per stellar generation (R) and the net stellar yield (y_{Si}) using the NuGrid collaboration yield set (Ritter et al. 2018b) and the SYGMA simple stellar population model (Ritter et al. 2018a). The definitions of R and y_{Si} follow those in Vincenzo et al. (2016). In Table A1, we show the R and y_{Si} values calculated with different choices of IMFs and metal mass fractions. For the calculation of each set of (Z , R , y_{Si}), we assume a minimum stellar mass of $0.08 M_{\odot}$ and a maximum of $100 M_{\odot}$. When compared with the results from Vincenzo et al. (2016), the value of R varies by ~ 10 – 30 per cent for a given IMF and Z , probably due to different choices of stellar yield sets and a different treatment of massive stars in the stellar evolution modelling.

Table A1. Stellar yields y_{Si} and gas return fraction R .

Z	R	y_{Si}
Kroupa IMF (Kroupa 2002)		
0.0001	0.343	0.00269
0.0010	0.342	0.00311
0.0060	0.347	0.00372
0.0100	0.349	0.00333
0.0200	0.349	0.00334
Salpeter IMF (Salpeter 1955)		
0.0001	0.228	0.00281
0.0010	0.227	0.00320
0.0060	0.230	0.0376
0.0100	0.232	0.00342
0.0200	0.232	0.00345

This paper has been typeset from a $\text{\TeX}/\text{\LaTeX}$ file prepared by the author.